ACSNANO

www.acsnano.org

ARTICLE

Spatiotemporal Mapping of Hole Nucleation and Growth during Block Copolymer Terracing with High-Speed Atomic Force Microscopy

Julia G. Murphy, Jonathan G. Raybin, Genevieve E. Ansay, and Steven J. Sibener*

Cite This: *ACS Nano* 2023, 17, 5644–5652

Read Online

ACCESS | Metrics & More | Article Recommendations | Supporting Information

ABSTRACT: As a platform for investigating two-dimensional phase separation, we track the structural evolution of block copolymer thin films during thermal annealing with environmentally controlled atomic force microscopy (AFM). Upon thermal annealing, block copolymer films with incommensurate thickness separate into a terraced morphology decorated with holes. With *in situ* imaging at 200 °C, we follow the continuous progression of terrace formation in a single region of a cylinder-forming poly(styrene-*block*-methyl methacrylate) thin film, beginning with the disordered morphology on an unpatterned silicon substrate and continuing through nucleation and coarsening stages. Topographic AFM imaging with nanoscale resolution simultaneously captures ensemble hole growth statistics while locally tracking polymer diffusion through measurements of the film thickness. At early times, we observe homogeneous hole nucleation and isotropic growth, with kinetics following the predictions of classical nucleation theory. At later times, however, we find anomalous hole growth which arises due to the combination of Ostwald ripening and coalescence mechanisms. In each case, our real-space observations highlight the importance of hole interactions for determining coarsening kinetics, mediated either through the interconnected phase for Ostwald ripening or through binary collision events for coalescence.

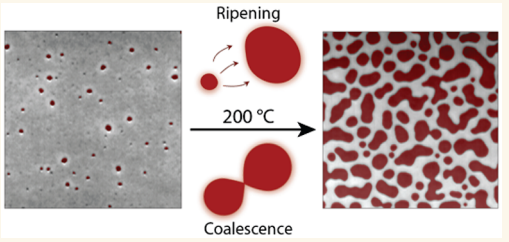

KEYWORDS: *atomic force microscopy, block copolymers, coalescence, nucleation and growth, Ostwald ripening, PS-b-PMMA, terracing*

INTRODUCTION

Across a diverse array of phenomena, activated phase transformations follow a consistent progression, featuring nucleation and growth at early times, followed by coarsening at late times. The evolution between these stages is a continuous process governed by a common set of thermodynamic relationships.[1,2] As described by classical nucleation theory (CNT), homogeneous nucleation events arise when localized fluctuations of the emerging phase exceed a threshold size, described by the critical radius, R_c. Fluctuations with radius $R < R_c$ are unstable and short-lived, as the energy penalty of the interface (which scales as R^2 in 3D or as R in 2D) outcompetes the favorable bulk energy of the new phase (which scales as R^3 or R^2, respectively). Droplets with $R > R_c$ grow over time, driving phase conversion until the system attains its equilibrium composition. At that stage, further reduction in free energy may be achieved by shrinking the interfacial area between phases through a droplet coarsening mechanism known as Ostwald ripening. As described by Lifshitz, Slyozov, and Wagner, each droplet maintains local equilibrium through the exchange of material with its surroundings, following the same detailed balance considerations as CNT.[3,4] Similar models have been developed that extend this description to 2D systems.[5] This capillarity-driven process results in the net transfer of material from smaller high-curvature droplets to larger low-curvature droplets. Over the same period, binary collisions between droplets can also lead to their coalescence, which further contributes to coarsening.[6] Together, these processes, which have each been thoroughly examined through theory, simulation, and experiment, provide a consistent and ubiquitous model for understanding phase transformations.[7−12]

Received: November 22, 2022
Accepted: March 6, 2023
Published: March 13, 2023

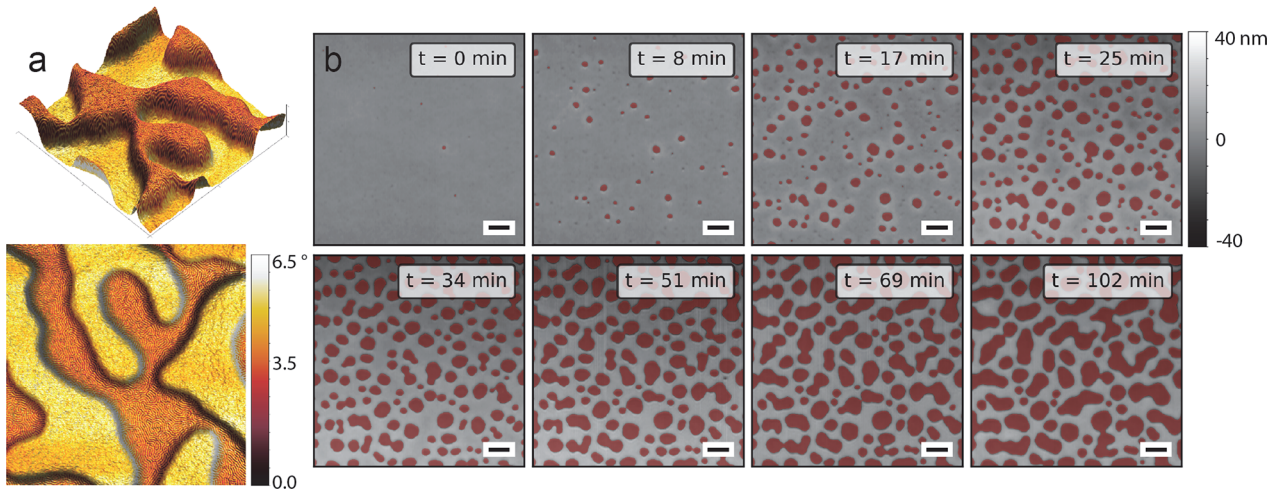

Figure 1. Terraced film morphology. (a) 3D perspective of the terraced PS-*b*-PMMA thin film topography, colored according to an overlaid AFM phase image to show compositional contrast. The lower terraces have uniform PS coverage at the air interface, while both PS and PMMA domains are present in the upper terraces, resulting in a striped fingerprint pattern. (b) Time series AFM images showing hole evolution over time. Nucleation sites are visible at the earliest imaging times, and these sites grow and merge over time. Hole regions are colored in red, and scale bars are 2 μm.

Block copolymer (BCP) thin films have frequently served as 2D platforms for studying nanoscale phase dynamics.[13] Due to microphase separation of the polymer domains, BCP films natively self-assemble into ordered, periodic nanopatterns with a natural length scale L_0, typically in the range 10−50 nm. For BCP confined to a substrate surface, the underlying nanoscale structure causes thin films to further organize on the mesoscale, forming terraced surfaces decorated with islands or holes.[14] Terracing occurs due to the layering of BCP nanopatterns into discrete levels with integral thicknesses τ, such that

$$\tau = \frac{1}{2} nL_0 \text{ where } n = 1,\ 2,\ 3,\ \ldots \quad (1)$$

When the thickness of a deposited film is incommensurate with L_0, i.e., for noninteger values of n, the free energy of the film may be reduced through phase separation into regions of upper and lower terraces that ensure local commensurability. During the terracing process, the film thickness serves as a globally conserved order parameter, and restructuring of the initially disordered morphology requires the diffusive transport of polymer chains through the film.

Although terracing dynamics in BCP films have been extensively studied, connecting measurements of the ensemble kinetics to local polymer transport mechanisms remains an important challenge. Depending on the initial film thickness, hole formation has been observed to occur through either nucleation or spinodal decomposition mechanisms.[15,16] In nearly commensurate thin films, terrace evolution proceeds through the nucleation of individual islands or holes distributed over the surface.[14] In highly incommensurate films, the greater initial stress drives thickness fluctuations that result in spinodal decomposition and the development of a bicontinuous terrace morphology.[17] Following the formation of relief structures, *in situ* optical microscopy of terrace coarsening has further identified that both coalescence and Ostwald ripening mechanisms contribute to their ongoing evolution.[18] The stress relaxation rate throughout these processes is limited by mass transport of the film. Optical methods, however, are not sensitive to local thickness gradients and therefore do not resolve specific transport mechanisms. By contrast, atomic force microscopy (AFM), which directly maps the nanoscale film topography, enables measurement of thickness variation within BCP layers. Observations of hole nucleation in BCP melts heated above the order−disorder transition temperature T_{ODT} find linear transport indicative of film slippage over the substrate interface,[6,19] similar to the dewetting behavior of viscoelastic homopolymer films.[20−22] In BCP films below T_{ODT}, however, negligible terrace slippage is observed and molecular descriptions instead predict diffusion-limited transport.[14,18] With *ex situ* AFM imaging of thermally quenched samples, Joly and co-workers observed the buildup of excess polymer surrounding the rim of the holes and suggested that diffusive transport of this material contributes to long-range interactions between holes and the onset of late-stage coarsening. The influence of diffusive hole interactions on terracing kinetics, however, has not been directly observed.

Here, we track the nucleation and growth of holes in terraced poly(styrene-*block*-methyl methacrylate) (PS-*b*-PMMA) thin films. Starting from an initially disordered film morphology, we use environmentally controlled AFM to heat the samples above the glass transition temperature and observe the phase separation to a terraced equilibrium state. These experiments capture the full temporal range of the transition, starting from the earliest stages of nucleation and growth and following through to late-stage coarsening. Through analysis of the growth statistics from these images, we see homogeneous nucleation and growth of the holes consistent with the expectations of CNT. At later stages, we find that coarsening occurs via a combination of simultaneous Ostwald ripening and coalescence mechanisms. In each case, real-space imaging reveals interactions between holes, mediated through either polymer diffusion in the interconnected terrace or binary merger events. Together these observations provide an explanation for anomalous power-law exponents in measurements of BCP terrace growth kinetics.

RESULTS AND DISCUSSION

We study the terracing dynamics of cylinder-forming PS-*b*-PMMA thin films, using BCP with a molecular weight of 77

https://doi.org/10.1021/acsnano.2c11672
ACS Nano 2023, 17, 5644−5652

kg/mol and 71 wt % PS composition. The resulting characteristic length scale of L_0 = 39.2 ± 2.5 nm was determined through measurement of the pattern periodicity, as described in the Supporting Information (Figure S1). Polymer films are prepared by spin-coating from toluene onto an unpatterned silicon wafer substrate, with an incommensurate average thickness of τ = 30.0 ± 0.2 nm measured by ellipsometry. Following deposition, the as-cast film morphology is far from equilibrium but is kinetically quenched, preventing terrace formation at room temperature. The film thickness was selected to fall within the range $\frac{1}{2}L_0 < \tau < L_0$ to ensure a nucleation and growth mechanism and single-layer terracing, such that the final structure after thermal annealing separates into holes with local thickness $\frac{1}{2}L_0$ and terraces with local thickness L_0. A 3D perspective of the terraced topography of a film after annealing is shown from two angles in Figure 1a with an overlaid phase color map. AFM phase imaging is sensitive to variation in the viscoelastic tip−surface interaction, providing contrast between PS and PMMA domains.[23] In this image, the lower terrace ($\frac{1}{2}L_0$) shows uniform PS coverage, while the upper terrace (L_0) is decorated by PS and PMMA stripes, indicative of BCP cylinders oriented parallel to the substrate.[24] At the silicon interface, PMMA interacts preferentially with the substrate, creating a $\frac{1}{2}L_0$ wetting layer with PS present at the air interface. Subsequent layers of PS-*b*-PMMA form cylindrical domains, with the first additional layer increasing the thickness by $\frac{1}{2}L_0$.[25] Because PS and PMMA have similar affinities for air, both components are present at the exposed interface and the top layer presents a characteristic striped morphology composed of PMMA cylinders embedded in the PS matrix.

Starting from an as-cast BCP film, we use environmentally controlled AFM to continuously image the terracing process. We image at 200 °C, which falls between the glass transition and order−disorder transition temperatures for PS-*b*-PMMA, in order to capture polymer dynamics *in situ*. Due to the weak temperature dependence of the Flory−Huggins interaction parameter for PS-*b*-PMMA, the choice of temperature controls the dynamic time scale without significantly influencing domain segregation or wetting behavior.[26,27] The film is heated in the AFM chamber to the set point temperature with a ramp rate of 1 °C s^{-1} immediately prior to AFM imaging. While heating, Ar flow is maintained over the sample to prevent oxygen exposure. In topography images, holes are observed to nucleate and grow over the course of imaging for roughly 2 h with a 26.2 s/image time resolution. Because we are primarily interested in mesoscale terrace dynamics, we image over a wide 20 μm × 20 μm field of view where we do not resolve the striped BCP pattern. The time series AFM data tracking hole formation are shown in Figure 1b, and the full movie is included as Supporting Information. Imaging data acquired over a smaller area with visible microdomain contrast, obtained on a separate film with similar thickness and under identical annealing conditions, are included in Figure S2.

From AFM imaging data, the hole area fraction over time is defined as $\Phi(t) = A(t)/A_{tot}$ where $A(t)$ is the hole area at time t and A_{tot} is the total imaging area. Following the lever rule, the film approaches an equilibrium hole coverage of

$$\Phi_{eq} = 2\left(1 - \frac{\tau}{L_0}\right) \tag{2}$$

corresponding to an expected value of Φ_{eq} = 0.48 for this system. We see the initial nucleation of the $\frac{1}{2}L_0$ level at discrete sites that grow isotropically over time, resulting in formation of circular holes within an interconnected terrace. When holes grow into the same area, they coalesce—often multiple, consecutive times—forming complex, irregular shapes. Continued coarsening of coalesced holes causes them to become rounder over time to minimize interfacial line tension. The relative terrace height measured in AFM is 19.8 ± 1.8 nm, consistent with a $\frac{1}{2}L_0$ height difference (Figure S3). AFM scratch tests following the *in situ* experiment find a height of 44.2 ± 1.8 nm of the upper terraces over the silicon substrate, confirming the $\frac{1}{2}L_0$: L_0 terrace structure.

Ensemble Kinetics. Over the course of thermal annealing, the BCP film follows a progression of stages on the road to equilibrium: (1) induction, (2) nucleation, and (3) coarsening. Each stage follows different growth kinetics and mechanisms and is therefore analyzed separately. Through each period, we track the appearance and development of holes over time, as displayed in Figure 2 on a logarithmic time scale including (a)

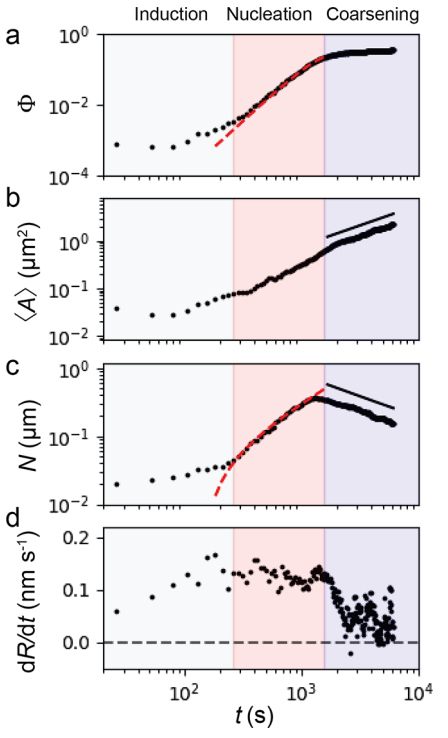

Figure 2. Ensemble hole growth statistics. Plots over time of the (a) total hole surface coverage Φ, (b) average area per hole ⟨*A*⟩, (c) number density of holes *N*, and (d) average hole growth rate ⟨d*R*/d*t*⟩. Three distinct periods are observed as the system progresses to equilibrium: induction (gray), nucleation (red), and coarsening (blue). The red dashed line in (a) shows a fit to the Avrami equation (eq 3) with fixed Avrami exponent *d* = 3 for 2D nucleation and growth. The red dashed line in (c) shows a linear regression of *N* over the same period. The black trend lines in (b) and (c) show power-law scaling with the exponents β = −0.62 and γ = 0.86 for the average area and number density during late-stage coarsening, respectively.

https://doi.org/10.1021/acsnano.2c11672
ACS Nano 2023, 17, 5644−5652

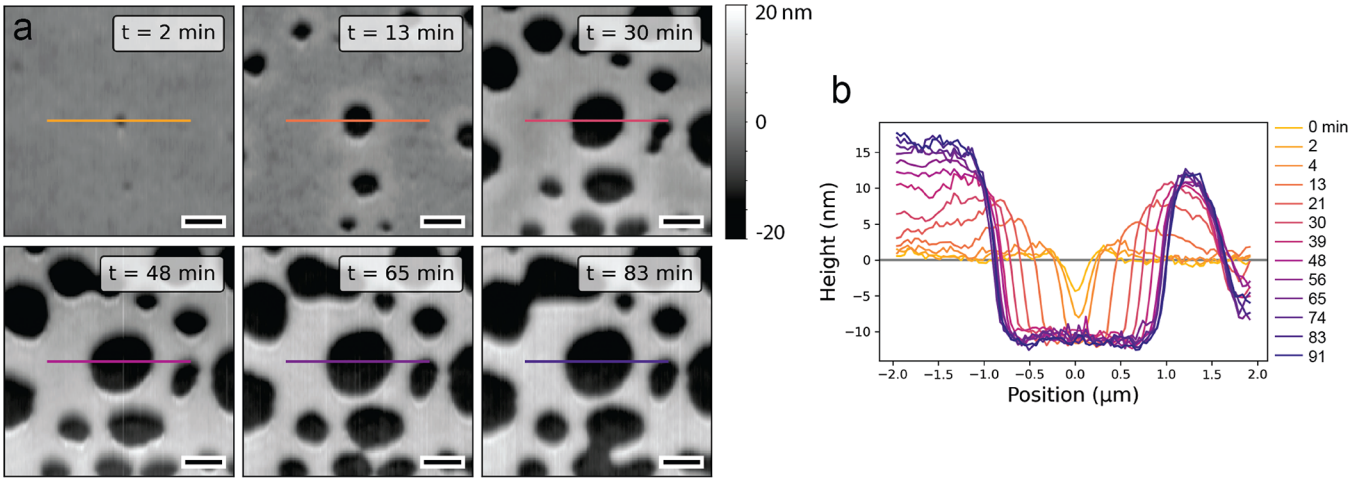

Figure 3. Nucleation and growth of an individual hole. (a) Time series AFM images tracking the growth of a single hole with (b) the corresponding topographic line profiles. The initial nucleation site grows down to a conical divot and then expands laterally, and an elevated halo around the hole propagates outward over the surrounding terrace. Scale bars are 1 μm.

the total hole surface coverage Φ, (b) the average area per hole $\langle A \rangle$, (c) the number density of holes N, and (d) the average hole growth rate $\left\langle \frac{dR}{dt} \right\rangle$. The same data plotted on a linear time scale are shown in Figure S4. For this analysis, we exclude holes touching the image boundary. In determining the growth rate, the area of each hole is related to an effective radius as $A = \pi R^2$, assuming circular holes, and the average growth rate is then calculated from the frame-to-frame change in radius for each hole.

At the beginning of AFM imaging, we observe a delay period prior to the onset of steady-state nucleation. This induction stage, highlighted in gray in Figure 2, has been previously described for BCP terracing and is indicative of an activation barrier for nucleation.[16] We capture only a portion of the full induction time following the initial AFM temperature ramp, due to the need for thermal equilibration before imaging. After the sample chamber reaches its set point temperature, the cantilever resonance changes and must be redetermined under the new thermal environment. Altogether, the polymer film is held above its glass transition temperature for approximately 5 min prior to imaging, and the first topographic AFM image, shown Figure 1b, therefore already includes sparse features distributed over the surface. At the onset of imaging, microphase separation of the PS and PMMA domains into a disordered nanopattern is also observed (Figure S2). The irregular domain structure suggests that many cylinder domains align perpendicular to the substrate to accommodate chain stretching at incommensurate thicknesses.[24] Polymer segregation involves only local segmental reorientation and therefore occurs on a shorter time scale than terracing, which requires diffusive chain transport over the film.

Following induction, the film enters the steady-state nucleation regime, indicated in red in Figure 2. As a measure of terracing kinetics, we apply Avrami analysis to quantify the hole area fraction $\Phi(t)$ (Figure 2a) following

$$\Phi(t) = \Phi_f[1 - \exp(-Kt^n)] \quad (3)$$

where Φ_f is the area fraction of holes at the end of the nucleation stage, K is the Avrami constant, and n is the Avrami exponent.[28] The Avrami equation (eq 3) describes the kinetics of phase transformations in the case of homogeneous nucleation and constant, isotropic growth. Under these assumptions, the Avrami exponent is related to dimensionality d of the growth process as $n = d + 1$, and, therefore, in our system $n = 3$. The red dashed line in the nucleation stage of Figure 2a corresponds to a least-squares fit of eq 3 with fixed $n = 3$, showing close agreement with the observed change in area fraction over this period. Throughout this period, we find that new holes are uniformly distributed in space and show a linear increase in number density over time, as indicated by the linear fit in Figure 2c. We also observe conformal hole growth that maintains roughly circular hole shapes with a constant radial growth rate of 0.124 ± 0.015 nm s^{-1} (Figure 2d). Altogether, these observations are consistent with the expected kinetics for homogeneous nucleation under CNT.

The end of the nucleation period, highlighted in blue in Figure 2, is identified by a slowdown of the terracing process. This transition marks the onset of late-stage coarsening, which is typically characterized by power-law scaling behavior. At this point new holes stop forming and existing holes begin to disappear, as evidenced by a turnover in N (Figure 2b), which decreases following $N \propto t^{\beta}$. At the same time, individual holes continue to grow and $\langle A \rangle$ increases following a power law $\langle A \rangle \propto t^{\gamma}$ (Figure 2c). The total hole coverage correspondingly scales as $\Phi \propto N\langle A \rangle \propto t^{\beta+\gamma}$,[6] and the positive balance of these exponents, with $\beta = -0.62$ and $\gamma = 0.86$, is indicative of ongoing phase conversion. At the onset of coarsening, the overall hole coverage fraction reaches $\Phi \sim 0.35$, still far from the expected equilibrium of $\Phi_{eq} = 0.48$, and continues to increase throughout the imaging period. Consistent with this observation, the average hole growth rate abruptly decreases at the beginning of the coarsening period but remains positive, approaching a rate of 0.05 ± 0.03 nm s^{-1} (Figure 2d).

The identification of power-law exponents is traditionally used to distinguish coarsening mechanisms.[6,29] For example, in the case of 2D Ostwald ripening, coarsening scales as $R \propto t^{1/3}$, and measurements of hole area correspondingly follow $A \propto R^2 \propto t^{2/3}$. Meanwhile, scaling laws for coalescence are predicted to follow a range of exponents, from $t^{1/4}$ to t^1, depending on the precise character of hole transport.[29] The observed $A \propto t^{0.86}$ scaling obtained from ensemble statistics, however, does not unambiguously establish a single coarsening mechanism. Instead, through direct observation of the growth process,

https://doi.org/10.1021/acsnano.2c11672
ACS Nano 2023, 17, 5644−5652

we see that the coarsening process occurs via two simultaneous mechanisms: Ostwald ripening and coalescence. Each process contributes to hole growth and decreases the total number of holes in the system: ripening through the evaporation of small holes and coalescence through hole merger events. The observed power-law exponents consequently reflect a combination of both concurrent mechanisms.

Diffusion-Limited Hole Growth. To better understand the growth process, we follow the evolution of an individual hole over time, beginning from its initial nucleation and continuing through the coarsening process, in time series AFM images (Figure 3a) and corresponding line profiles (Figure 3b). Hole nucleation and growth is driven by equilibration of the BCP film, which is initially unstable due to the incommensurability of the film thickness. At the earliest imaging times, we see evidence of an initial depression in the polymer film. This nucleation site develops into a conical divot, with the depth increasing over time until the base of the hole reaches a commensurate half-layer thickness. From there, the hole continues to expand laterally and isotropically, such that its center-of-mass position remains stationary. As the hole expands, a halo of excess material builds up around the rim during the initial growth stage.[19] In BCP films, halo formation is indicative of domain restructuring into a layered morphology, propagating from hole edges.[30]

Topographic AFM imaging enables investigation of chain transport and stress relaxation dynamics associated with reorganization of the BCP film. Variations in the film thickness provide a direct spatiotemporal map of local polymer concentration gradients. In Figure 4a, we track the evolution of the radial terrace profile surrounding the hole shown in Figure 3, following the relative position of the edge over time. Note that due to the asymmetric shape of the hole, we directly compare the distance of each pixel to the hole boundary, rather than performing an azimuthal integration. These profiles show the buildup of excavated polymer material around the rim of the hole that increases and spreads out over time. We measure the kinetics of chain transport by tracking the mean-squared displacement of the peak thickness R^2_{peak} over time (Figure 4b). The displacement R_{peak} is measured as the mean radial distance from the peak to the hole center-of-mass. For diffusion-controlled processes, we expect linear mean-squared expansion following

$$R^2_{peak} = 2Dt \tag{4}$$

Growth kinetics initially follow this trend, indicating diffusion-limited relaxation with a self-diffusion coefficient $D = 2.46(3) \times 10^{-12}$ cm^2 s^{-1}, consistent with previously reported measurements of PS-*b*-PMMA chain diffusion with the same molecular weight and composition.[31] These observations confirm that chain diffusion governs transport kinetics, in contrast with the dewetting of BCP melts annealed above T_{ODT}, where substrate slippage leads to bulk transport following $R \propto t$.[6,20] At late times, the apparent rim migration rate slows, as polymer diffusion from neighboring holes also begins to contribute to the local thickness.

As excess material expands around hole boundaries, the thickness of the surrounding terrace stabilizes, and polymer concentration gradients achieve a steady state. The peak terrace thickness (Figure 4c) increases over time and begins to plateau as the surrounding terrace approaches equilibrium. The observed leveling of the terrace line profile in Figure 4a

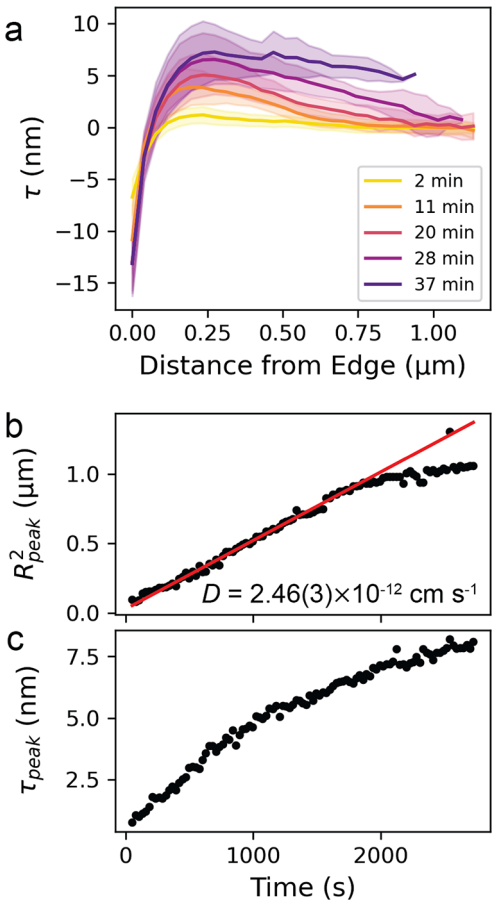

Figure 4. Terrace leveling and diffusion. (a) Film thickness as a function of distance from the hole edge showing leveling of the surrounding terrace over time. (b) Mean-squared displacement R^2_{peak} of the terrace peak from the hole center over time. The red line shows a linear regression indicating diffusion-limited kinetics during nucleation, which deviates due to the interaction of surrounding holes at late times. (c) The peak film thickness increases, approaching a plateau as the terrace thickness levels.

coincides with the onset of late-stage coarsening. At this point, hole growth becomes sensitive to the surrounding hole environment, with interactions mediated through chain diffusion in the upper terrace, and, at the same time, we no longer observe the formation of new nuclei. Hole nucleation is an activated process driven by the transport and relaxation of stretched chains within incommensurate regions and stops once the terrace achieves a stable, commensurate thickness.

Hole Interactions and Coarsening Mechanisms. Following the steady-state nucleation period, real-space imaging reveals concurrent Ostwald ripening and coalescence mechanisms leading to droplet coarsening. To understand the separate contributions of these mechanisms, we now examine each of these processes in more detail.

During Ostwald ripening, holes maintain equilibrium with the surrounding terrace environment through the exchange of individual polymer chains at the hole edges. As part of this process, hole coarsening proceeds through an evaporation–condensation mechanism driven by the instability of small, high-curvature holes relative to large, low-curvature holes. Accordingly, alongside instances of hole growth, we also observe cases where smaller holes shrink and disappear. As an example, a time series showing the formation and subsequent

https://doi.org/10.1021/acsnano.2c11672
ACS Nano 2023, 17, 5644–5652

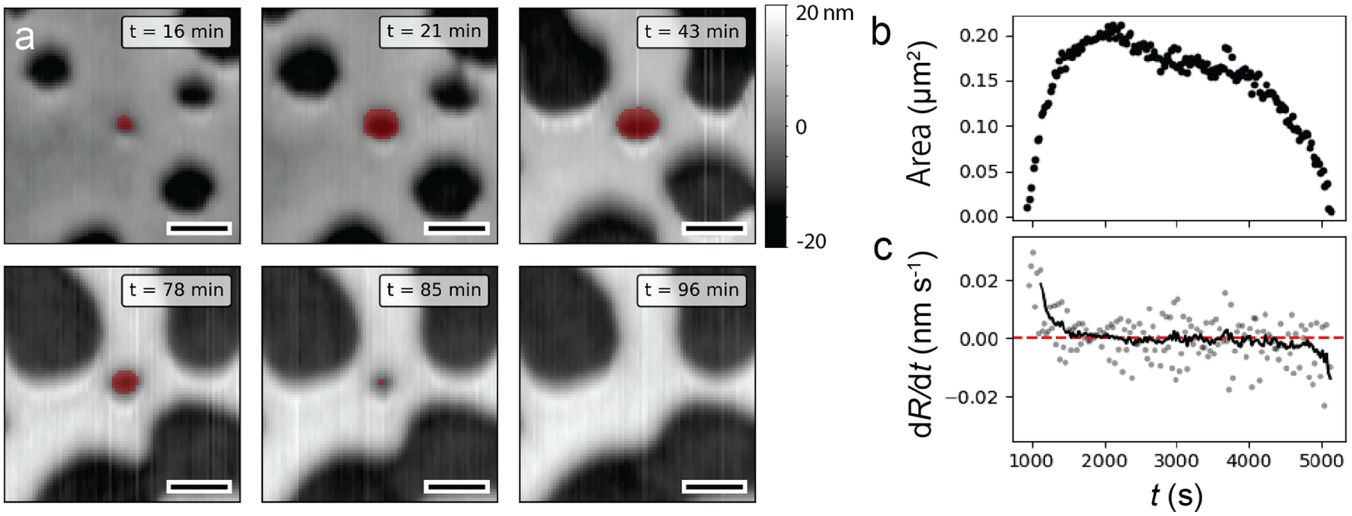

Figure 5. Ostwald ripening and hole evaporation. (a) Time series AFM images of the disappearance of a hole (red) due to Ostwald ripening. (b) Plot of the area of the highlighted hole over time. The hole area initially increases at early times and eventually decreases at late times due to the changing critical radius, before vanishing completely. (c) Plot of the frame-to-frame growth rate of the highlighted hole. The black curve shows a rolling average of the growth rate over a 7 frame window. Scale bars are 1 μm.

disappearance of a hole is shown in Figure 5a. During the initial nucleation and growth period, the hole grows along with its neighbors. At the onset of coarsening, the hole area then plateaus and begins to decrease before completely vanishing (Figure 5b). Over this period, the frame-to-frame growth rate crosses from positive to negative values (Figure 5c).

The reversal in hole growth occurs due to changes in local stress of the surrounding environment over time.[14] Initially, during nucleation and growth, the system is far from equilibrium and large stress gradients drive stretched polymer chains to detach from the hole edge and flow to the surrounding terrace. As the terrace thickness stabilizes, the relaxation of the upper terrace region leads to slower overall hole growth. Through this process, the critical radius for hole stability also increases over time, outpacing some fraction of smaller holes. Holes that fall below the critical radius, such as the one shown in Figure 5a, become unstable, shrink, and ultimately disappear as chains reattach to their boundary.

To measure the change in critical radius, we compare the size dependence of the average hole growth rate between the early stage nucleation and growth and late-stage coarsening. From statistical analysis of the frame-to-frame change in radius of each hole, we measure the fraction of holes that grow (ρ_g) and shrink ($\rho_s = 1 - \rho_g$) as a function of radius over each stage.[8,32] The net growth probability ($\rho_g - \rho_s$) initially increases from negative to positive, with the crossover marking the critical radius R_c, and levels off for sufficiently large holes (Figure 6a). At late times, the difference $\rho_g - \rho_s$ is generally smaller, and the crossover shifts to larger radii, consistent with slowing hole growth rates. Between these stages, the critical radius increases from $R_c = 39 \pm 20$ nm to $R_c = 137 \pm 20$ nm.

Similar trends are observed in plots of the average growth rate as a function of radius (Figure 6b), with a crossover from negative to positive growth at the critical radius. The growth rate peaks shortly above the critical radius and then decreases asymptotically at large radii. As with measurements of the growth probability, the average growth rate is generally lower at late times. In the case of diffusion-controlled growth, the growth rate of an individual hole may be determined from the Gibbs−Thomson equation and follows a size-dependence:

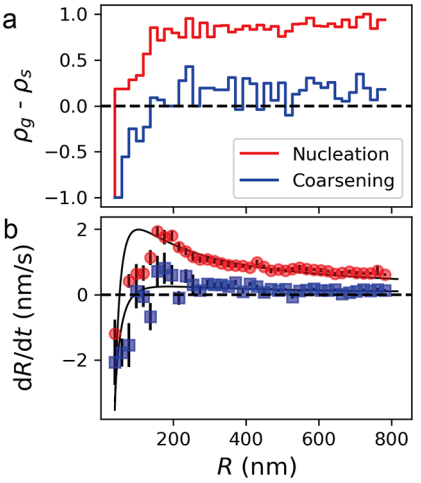

Figure 6. Evolution of the critical radius. (a) The probability difference $\rho_g - \rho_s$ for holes to grow and shrink as a function of hole radius during nucleation (red) and coarsening (blue) periods. Growth is slower at late times, and the critical radius, which corresponds to the crossover from negative to positive, also increases. (b) Comparison of the average hole growth rate as a function of hole radius over each time period. The black trend lines show fits to eq 4.

$$\frac{dR}{dt} = \frac{K_D}{R}\left(\frac{1}{R_c} - \frac{1}{R}\right) \tag{5}$$

where K_D is a constant proportional to the chain diffusion constant.[33−35] Although fits to eq 5 recover these qualitative trends, we find significant deviation at small hole sizes. Crucially, this expression assumes conformal growth, which does not hold for noncircular holes observed at late times. Moreover, this analysis assumes the independent growth of individual, isolated holes and does not account for hole interactions or heterogeneity. Still, differences in the size-dependent growth between each stage provide statistical confirmation of the time evolution of R_c.

https://doi.org/10.1021/acsnano.2c11672
ACS Nano 2023, 17, 5644−5652

Alongside Ostwald ripening, we observe discrete binary hole mergers via a coalescence mechanism. Coalescence events, which occur when two holes converge, become more frequent as the total hole coverage increases and often recur multiple times for a given hole. Repeated mergers give rise to the irregular, noncircular hole shapes observed at late times.[18] One example of a hole merger is shown in Figure 7a, in which two

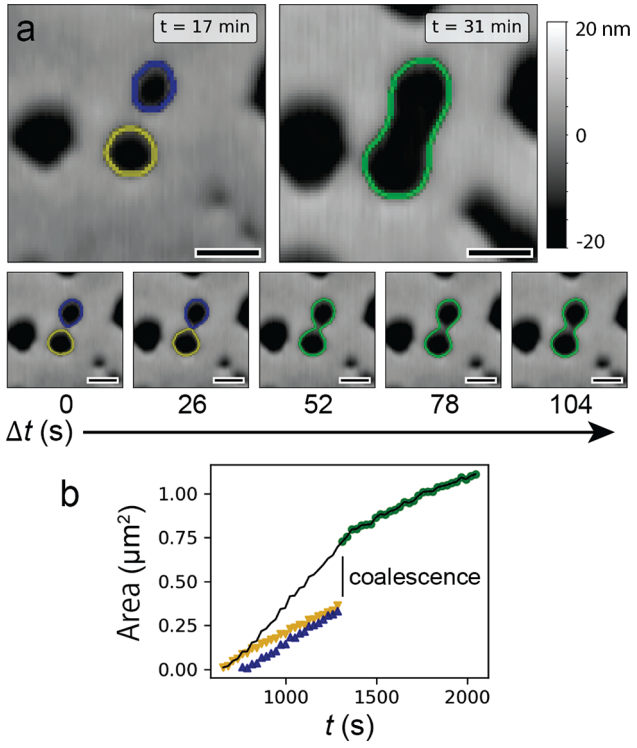

Figure 7. Hole coalescence. (a) Time series AFM images capturing a merger event between two holes. The top images show the holes before (left) and after (right) coalescence, while the image series (bottom) shows the frame-to-frame progression of the coalescence mechanism through time. The perimeter of each hole is highlighted along contours of constant height. (b) Plots of the total area and area of the highlighted holes, with colors corresponding to panel (a). Scale bars are 500 nm.

individual holes, outlined in blue and yellow, grow into the same region of space. As the holes approach, the bridge region separating them becomes unstable, and they coalesce into a single larger hole with a peanut shape, outlined in green. At this point, hole growth becomes concentrated at the high-curvature neck due to the Gibbs−Thomson effect, and the neck widens over time until the hole recovers a circular shape that minimizes line tension along the hole boundary. The overall terrace shape evolution is governed by a competition between this thermodynamically favored path toward circularity and kinetically controlled merger events.

We track the area of the component holes through this process in Figure 7b. This plot provides an illustration of the scaling behavior of hole growth, which slows with increasing area. The larger (yellow) hole initially grows more slowly than the smaller (blue) hole. After they merge, the total growth rate abruptly decreases due to the larger size of the new combined hole (green).

In this system, mergers occur when nearest-neighbor holes grow into each other. Over experimental time scales, we find negligible center-of-mass motion, such that hole diffusion and drift do not contribute to the coalescence rate (Figure S5).[36] As two holes approach, the narrow bridge region that separates them is destabilized by the proximity of both hole boundaries.[37] The localized interfacial tension of this geometry establishes a pressure gradient that drives flow from narrow regions to wide regions in the interconnected phase, and, in fluid systems, the resulting hydrodynamic currents often further drive droplet motion.[29,38] The diffusion-limited dynamics of the polymer melt studied here limits long-range flow, and we expect that hydrodynamic currents only disrupt the bridge locally, where curvature is highest.[39]

The combined contributions of Ostwald ripening and coalescence together yield anomalous power-law exponents that exceed the predicted rate for capillarity-driven growth alone. Because we visualize the real-space mechanism for each process, we can distinguish discrete merger events from continuous growth due to ripening. In this manner, we consider the separate contributions of each mechanism to hole disappearance and growth during coarsening (Figure S6). Hole disappearance is primarily driven by coalescence, with the number of mergers exceeding evaporations by roughly an order of magnitude. Conversely, hole growth is primarily determined by continuous ripening processes over the course of the experiment. In general, coalescence becomes increasingly significant at late times, as the increasing hole fraction shortens typical hole separation distances, and, extrapolated to longer imaging times, growth due to coalescence is expected to outpace ripening.

In our estimate of the separated growth rate excluding mergers, we find a power-law scaling of $\langle A \rangle \sim t^{1/2}$, corresponding with $R \sim t^{1/4}$ and smaller than the predicted $R \sim t^{1/3}$ scaling for Ostwald ripening. This discrepancy underscores a limitation of the separation procedure. Coupling between ripening and coalescence processes introduces cross-interactions, such that the hole growth rate is not a simple additive sum.[36] For instance, ripening dynamics are modified by coalescence due to the changing size and shape of holes. In particular, we expect that ripening is slowed, because merger events cause holes to grow larger at earlier times. Moreover, the coalescence rate is entirely dependent on ripening kinetics, as mergers only occur when continuous growth causes neighboring holes to expand into each other. Altogether, real-space imaging reveals how the interplay between these processes contributes to coarsening dynamics.

Understanding terracing kinetics is a critical component in controlling the hierarchical self-assembly of BCP film morphologies. The terrace structure can be engineered using lithography to modulate the substrate chemistry or topography, employing directed self-assembly approaches commonly used to guide the BCP nanopattern to also influence the mesoscale terrace structure.[13] On topographically patterned substrates, capillary flow from high to low regions leads to thickness variations that can be used to induce the formation of relief structures at specified locations.[40,41] Chemical patterning of the substrate may also be used to tune the relative wetting energies of each domain, providing control over domain orientation while also templating variations in the film thickness.[42] This control over the terrace morphology offers the potential for selective, localized functionalization of BCP surfaces.[43] Moreover, control over the evolution of the terrace topography can in turn be used to drive nanopattern ordering through flow-induced alignment.[39] In each case, the

https://doi.org/10.1021/acsnano.2c11672
ACS Nano 2023, 17, 5644−5652

mesoscale terrace architecture is intrinsically connected to thermodynamics of the nanoscale pattern.

CONCLUSION

Environmentally controlled and high-speed AFM has enabled *in situ* characterization of hole nucleation and growth kinetics in terraced BCP thin films. By tracking the film topography in real time and space, we establish direct connections between the ensemble hole statistics and associated growth mechanisms. Over the course of annealing, we identify varying kinetic behavior associated with distinct growth mechanisms for the nucleation and coarsening stages. We find that the transition between these stages is signaled by the diffusion-limited leveling of the upper terrace surrounding the holes. At each stage, holes experience different terrace environments and therefore demonstrate different growth kinetics, exemplified by an increase in the critical radius from 39 ± 20 nm to 137 ± 20 nm. We further observe that the combination of Ostwald ripening (through an evaporation−condensation mechanism) and coalescence (through binary hole collisions) concurrently contributes to coarsening, leading to anomalous power law scaling. Altogether, these measurements demonstrate the utility of high-speed AFM for connecting the evolution of the mesoscale film topography to the underlying nanoscale structure. Looking forward, this platform offers additional potential for characterizing the effects of polymer transport—including flow-induced domain alignment—on lithographically patterned substrates used for the directed self-assembly of BCP films.

METHODS

Samples were prepared on silicon wafer substrates from Virginia Semiconductor, Inc. Wafers were cleaned by sonicating in toluene and then acetone for 5 min each, then rinsed with isopropanol and dried with N_2. Cylinder-forming PS-*b*-PMMA with a molecular weight of 77 kg/mol and 29% PS was purchased from Polymer Source, Inc., and prepared in 0.9 wt % solutions in toluene. The solution was spin-cast onto the cleaned substrates at 3000 rpm for 60 s to obtain the desired film thickness. The average film thickness was measured on a Gaertner Waferskan ellipsometer, with an estimated index of refraction of 1.53, and found to be 30.0 ± 0.2 nm.

High-speed tapping mode AFM imaging was performed on an Asylum Research Cypher ES Environmental AFM, using FS-1500 cantilevers with 1.5−2.0 MHz resonant frequency and a set point of 500 mV to prevent sample damage during scanning. As-cast samples were heated *in situ* to 200 °C at a ramp rate of 1 °C s^{-1}. While annealing, a stream of Ar gas was flowed through the sample chamber with an overpressure of 30−40 mbarg to ensure an oxygen-free environment. Upon reaching the set point temperature, the cantilever resonance was redetermined prior to imaging. The sample was then imaged continuously with a line scan rate of 19.53 Hz with 512 × 512 pixel resolution over a 20 μm × 20 μm area, giving an overall imaging rate of 26.2 s per image.

AFM images were processed and analyzed using custom Python code. Images were flattened and filtered with a Gaussian blur to remove imaging artifacts using the SPIEPy package. Terrace boundaries were identified through local height thresholding, excluding holes that touch the image edges, and analyzed using the scipy library.[44] Frame-to-frame linking of holes was performed by tracking their center-of-mass positions using the trackpy implementation of the Crocker−Grier algorithm.[45,46]

ASSOCIATED CONTENT

Supporting Information

The Supporting Information is available free of charge at https://pubs.acs.org/doi/10.1021/acsnano.2c11672.

Figures S1−S6 containing measurement of L_0; measurement of the terrace thickness; ensemble growth statistics on a linear time scale; observations of the appearance and evolution of cylinder domains; analysis of hole center-of-mass trajectories; and analysis of the relative contribution of coalescence mechanisms (PDF)

Video S1: movie of the AFM time series data showing hole growth processes during thermal annealing, with holes highlighted in red (MP4)

AUTHOR INFORMATION

Corresponding Author

Steven J. Sibener − *Department of Chemistry and The James Franck Institute, The University of Chicago, Chicago, Illinois 60637, United States;* orcid.org/0000-0002-5298-5484; Phone: 773-702-7193; Email: s-sibener@uchicago.edu

Authors

Julia G. Murphy − *Department of Chemistry and The James Franck Institute, The University of Chicago, Chicago, Illinois 60637, United States*

Jonathan G. Raybin − *Department of Chemistry and The James Franck Institute, The University of Chicago, Chicago, Illinois 60637, United States;* Present Address: Department of Chemistry, University of California Berkeley, Berkeley, California 94720, United States

Genevieve E. Ansay − *Department of Chemistry and The James Franck Institute, The University of Chicago, Chicago, Illinois 60637, United States*

Complete contact information is available at: https://pubs.acs.org/10.1021/acsnano.2c11672

Notes

The authors declare no competing financial interest.

ACKNOWLEDGMENTS

This work was supported by the U.S. Department of Commerce, National Institute of Standards and Technology, as part of the Center for Hierarchical Materials Design (CHiMaD), under award no. 70NANB19H005. J.G.M. and S.J.S. acknowledge support from the National Science Foundation grant CHE-1900188, including an NSF Alliances for Graduate Education and Professoriate supplement. We also thank the Advanced Materials for Energy-Water Systems (AMEWS) Center, an Energy Frontier Research Center funded by the US Department of Energy, Office of Science, Basic Energy Sciences. AFM measurements and sample preparation were supported by the NSF Materials Research Science and Engineering Center (MRSEC) at the University of Chicago, grant no. NSF-DMR-2011854.

REFERENCES

(1) Sagui, C.; Grant, M. Theory of nucleation and growth during phase separation. *Phys. Rev. E* **1999**, *59*, 4175−4187.

(2) Wu, S.; Li, M.; Sun, Y. In Situ Synchrotron X-ray Characterization Shining Light on the Nucleation and Growth Kinetics of Colloidal Nanoparticles. *Angew. Chem., Int. Ed.* **2019**, *58*, 8987−8995.

(3) Lifshitz, I. M.; Slyozov, V. V. The kinetics of precipitation from supersaturated solid solutions. *J. Phys. Chem. Solids* **1961**, *19*, 35−50.
(4) Wagner, C. Theorie der Alterung von Niederschlägen durch Umlösen (Ostwald-Reifung). *Zeitschrift für Elektrochemie, Berichte der Bunsengesellschaft für physikalische Chemie* **1961**, *65*, 581−591.
(5) Ardell, A. J. Late-stage two-dimensional coarsening of circular clusters. *Phys. Rev. B* **1990**, *41*, 2554−2556.
(6) Limary, R.; Green, P. F. Dynamics of Droplets on the Surface of a Structured Fluid Film: Late-Stage Coarsening. *Langmuir* **2003**, *19*, 2419−2424.
(7) Leptoukh, G.; Strickland, B.; Roland, C. Phase Separation in Two-Dimensional Fluid Mixtures. *Phys. Rev. Lett.* **1995**, *74*, 3636−3639.
(8) Gasser, U.; Weeks, E. R.; Schofield, A.; Pusey, P. N.; Weitz, D. A. Real-Space Imaging of Nucleation and Growth in Colloidal Crystallization. *Science* **2001**, *292*, 258−262.
(9) Haußer, F.; Voigt, A. Ostwald ripening of two-dimensional homoepitaxial islands. *Phys. Rev. B* **2005**, *72*, 035437.
(10) De Yoreo, J. J.; Gilbert, P. U. P. A.; Sommerdijk, N. A. J. M.; Penn, R. L.; Whitelam, S.; Joester, D.; Zhang, H.; Rimer, J. D.; Navrotsky, A.; Banfield, J. F.; Wallace, A. F.; Michel, F. M.; Meldrum, F. C.; Cölfen, H.; Dove, P. M. Crystallization by particle attachment in synthetic, biogenic, and geologic environments. *Science* **2015**, *349*, aaa6760.
(11) Hueckel, T.; Hocky, G. M.; Palacci, J.; Sacanna, S. Ionic solids from common colloids. *Nature* **2020**, *580*, 487−490.
(12) Fernández-Rico, C.; Sai, T.; Sicher, A.; Style, R. W.; Dufresne, E. R. Putting the Squeeze on Phase Separation. *JACS Au* **2022**, *2*, 66−73.
(13) Darling, S. B. Directing the self-assembly of block copolymers. *Prog. Polym. Sci.* **2007**, *32*, 1152−1204.
(14) Grim, P. C. M.; Nyrkova, I. A.; Semenov, A. N.; ten Brinke, G.; Hadziioannou, G. The Free Surface of Thin Diblock Copolymer Films: Experimental and Theoretical Investigations on the Formation and Growth of Surface Relief Structures. *Macromolecules* **1995**, *28*, 7501−7513.
(15) Coulon, G.; Daillant, J.; Collin, B.; Benattar, J. J.; Gallot, Y. Time evolution of the free surface of ultrathin copolymer films. *Macromolecules* **1993**, *26*, 1582−1589.
(16) Peters, R. D.; Dalnoki-Veress, K. Film thickness dependent ordering dynamics of lamellar forming diblock copolymer thin films. *Eur. Phys. J. E* **2012**, *35*, 132.
(17) Peters, R. D.; Stasiak, P.; Matsen, M. W.; Dalnoki-Veress, K. Morphology Induced Spinodal Decomposition at the Surface of Symmetric Diblock Copolymer Films. *ACS Macro Lett.* **2013**, *2*, 441−445.
(18) Coulon, G.; Collin, B.; Ausserre, D.; Chatenay, D.; Russell, T. Islands and holes on the free surface of thin diblock copolymer films. I. Characteristics of formation and growth. *J. Phys. (Paris)* **1990**, *51*, 2801−2811.
(19) Limary, R.; Green, P. F. Dewetting Instabilities in Thin Block Copolymer Films: Nucleation and Growth. *Langmuir* **1999**, *15*, 5617−5622.
(20) Brochard-Wyart, F.; Debregeas, G.; Fondecave, R.; Martin, P. Dewetting of Supported Viscoelastic Polymer Films: Birth of Rims. *Macromolecules* **1997**, *30*, 1211−1213.
(21) Stange, T. G.; Evans, D. F.; Hendrickson, W. A. Nucleation and Growth of Defects Leading to Dewetting of Thin Polymer Films. *Langmuir* **1997**, *13*, 4459−4465.
(22) Mukherjee, R.; Sharma, A. Instability, self-organization and pattern formation in thin soft films. *Soft Matter* **2015**, *11*, 8717−8740.
(23) Cleveland, J. P.; Anczykowski, B.; Schmid, A. E.; Elings, V. B. Energy dissipation in tapping-mode atomic force microscopy. *Appl. Phys. Lett.* **1998**, *72*, 2613−2615.
(24) Zucchi, I. A.; Poliani, E.; Perego, M. Microdomain orientation dependence on thickness in thin films of cylinder-forming PS-b-PMMA. *Nanotechnology* **2010**, *21*, 185304.
(25) Zhang, X.; Berry, B. C.; Yager, K. G.; Kim, S.; Jones, R. L.; Satija, S.; Pickel, D. L.; Douglas, J. F.; Karim, A. Surface Morphology Diagram for Cylinder-Forming Block Copolymer Thin Films. *ACS Nano* **2008**, *2*, 2331−2341.
(26) Russell, T. P.; Hjelm, R. P. J.; Seeger, P. A. Temperature dependence of the interaction parameter of polystyrene and poly(methyl methacrylate). *Macromolecules* **1990**, *23*, 890−893.
(27) Seguini, G.; Zanenga, F.; Cannetti, G.; Perego, M. Thermodynamics and ordering kinetics in asymmetric PS- b -PMMA block copolymer thin films. *Soft Matter* **2020**, *16*, 5525−5533.
(28) Svoboda, R. Crystallization of glasses - When to use the Johnson-Mehl-Avrami kinetics? *Journal of the European Ceramic Society* **2021**, *41*, 7862−7867.
(29) Haas, C. K.; Torkelson, J. M. Two-dimensional coarsening and phase separation in thin polymer solution films. *Phys. Rev. E* **1997**, *55*, 3191−3201.
(30) Joly, S.; Ausserré, D.; Brotons, G.; Gallot, Y. Hole nucleation in thin diblock copolymer films. *Eur. Phys. J. E* **2002**, *8*, 355−363.
(31) Tong, Q.; Sibener, S. J. Visualization of Individual Defect Mobility and Annihilation within Cylinder-Forming Diblock Copolymer Thin Films on Nanopatterned Substrates. *Macromolecules* **2013**, *46*, 8538−8544.
(32) Zhan, G.; Cai, Z.-F.; Strutyński, K.; Yu, L.; Herrmann, N.; Martínez-Abadía, M.; Melle-Franco, M.; Mateo-Alonso, A.; Feyter, S. D. Observing polymerization in 2D dynamic covalent polymers. *Nature* **2022**, *603*, 835−840.
(33) Sugimoto, T. Preparation of monodispersed colloidal particles. *Adv. Colloid Interface Sci.* **1987**, *28*, 65−108.
(34) Peng, X.; Wickham, J.; Alivisatos, A. P. Kinetics of II-VI and III-V Colloidal Semiconductor Nanocrystal Growth: "Focusing" of Size Distributions. *J. Am. Chem. Soc.* **1998**, *120*, 5343−5344.
(35) Talapin, D. V.; Rogach, A. L.; Haase, M.; Weller, H. Evolution of an Ensemble of Nanoparticles in a Colloidal Solution: Theoretical Study. *J. Phys. Chem. B* **2001**, *105*, 12278−12285.
(36) Conti, M.; Meerson, B.; Peleg, A.; Sasorov, P. V. Phase ordering with a global conservation law: Ostwald ripening and coalescence. *Phys. Rev. E* **2002**, *65*, 046117.
(37) Backholm, M.; Benzaquen, M.; Salez, T.; Raphaël, E.; Dalnoki-Veress, K. Capillary levelling of a cylindrical hole in a viscous film. *Soft Matter* **2014**, *10*, 2550.
(38) Aarts, D. G. A. L.; Lekkerkerker, H. N. W.; Guo, H.; Wegdam, G. H.; Bonn, D. Hydrodynamics of Droplet Coalescence. *Phys. Rev. Lett.* **2005**, *95*, 164503.
(39) Zhang, H.; Wang, B.; Wang, G.; Shen, C.; Chen, J.; Reiter, G.; Zhang, B. Dewetting-Induced Alignment and Ordering of Cylindrical Mesophases in Thin Block Copolymer Films. *Macromolecules* **2020**, *53*, 9631−9640.
(40) Segalman, R. A.; Schaefer, K. E.; Fredrickson, G. H.; Kramer, E. J.; Magonov, S. Topographic Templating of Islands and Holes in Highly Asymmetric Block Copolymer Films. *Macromolecules* **2003**, *36*, 4498−4506.
(41) Park, S.; Tsarkova, L.; Hiltl, S.; Roitsch, S.; Mayer, J.; Böker, A. Guiding Block Copolymers into Sequenced Patterns via Inverted Terrace Formation. *Macromolecules* **2012**, *45*, 2494−2501.
(42) Peters, R. D.; Yang, X. M.; Nealey, P. F. Morphology of Thin Films of Diblock Copolymers on Surfaces Micropatterned with Regions of Different Interfacial Energy. *Macromolecules* **2002**, *35*, 1822−1834.
(43) Raybin, J. G.; Sibener, S. J. In Situ Visualization of Solvent Swelling Dynamics in Block Copolymer Films with Atomic Force Microscopy. *Macromolecules* **2019**, *52*, 5985−5994.
(44) Virtanen, P.; et al. SciPy 1.0: Fundamental Algorithms for Scientific Computing in Python. *Nat. Methods* **2020**, *17*, 261−272.
(45) Wel, C. V. D.; Allan, D.; Keim, N.; Caswell, T. Trackpy: Fast, Flexible Particle-Tracking Toolkit. http://soft-matter.github.io/trackpy/v0.5.0/, accessed March 2, 2023.
(46) Crocker, J. C.; Grier, D. G. Methods of Digital Video Microscopy for Colloidal Studies. *J. Colloid Interface Sci.* **1996**, *179*, 298−310.

https://doi.org/10.1021/acsnano.2c11672
ACS Nano 2023, 17, 5644−5652